A broadband cavity-enhanced spectrometer for atmospheric trace gas measurements and Rayleigh scattering cross sections in the cyan region (470-540 nm)

5   Nick Jordan,[1] Connie Z. Ye,[1] Satyaki Ghosh,[1] Rebecca A. Washenfelder,[2] Steven S. Brown,[2] and Hans D. Osthoff[1]

[1] Department of Chemistry, University of Calgary, 2500 University Drive NW, Calgary, AB T2N 1N4, Canada

[2] Earth System Research Laboratory, National Oceanic and Atmospheric Administration, 325 Broadway, Boulder,
10   CO 80303, USA

Correspondence: Hans D. Osthoff (hosthoff@ucalgary.ca)

Abstract. A cavity-enhanced absorption spectrometer (CEAS) for quantification of atmospheric trace gases that absorb in the cyan region of the electromagnetic spectrum (470 to 540 nm), including NO_2 and I_2, is described. The instrument uses a light-emitting diode coupled to a 1 m optical cavity consisting of a pair of mirrors in stable resonator
15   configuration. Transmitted light is monitored using a grating spectrometer and charge-coupled device array detector. The average mirror reflectivity was determined from the N_2/He and Ar/He ratios of scattering coefficients and was ~99.98% at its maximum, yielding an effective optical path length of 6.3 km. Cross-sections of N_2, O_2, air, Ar, CO_2, and CH_4 scattering and of O_4 absorption were measured and agree with literature values within the measurement uncertainty. Trace gas mixing ratios were retrieved using the spectral fitting software DOASIS from 480 to 535 nm.
20   Under laboratory conditions, the 60 s, 1σ measurement precisions were ±105 and ±38 pptv for NO_2 and I_2, respectively. The CEAS sampled ambient air in Ucluelet, BC, in July 2015. CEAS retrievals agreed with independent measurements of NO_2 by blue diode laser cavity ring-down spectroscopy (r^2 = 0.975), but ambient I_2 concentrations were below the detection limit.

Keywords: Cavity-enhanced spectroscopy, cyan region, Rayleigh scattering cross-sections, atmospheric trace gas
25   measurements, nitrogen dioxide, iodine

1 Introduction

Broadband cavity-enhanced absorption spectroscopy (CEAS) has emerged in recent years as a sensitive technique for direct measurement of atmospheric trace gases (Fiedler et al., 2003; Gherman et al., 2008; Vaughan et al., 2008; Washenfelder et al., 2008; Schuster et al., 2009; Thalman and Volkamer, 2010; Hoch et al., 2014) and of aerosol
30   optical extinction (Thalman and Volkamer, 2010; Bluvshtein et al., 2012; Washenfelder et al., 2013). Similar to other cavity-enhanced techniques (Gagliardi and Loock, 2014), CEAS owes its high sensitivity to highly reflective mirrors (reflectivity, R > 99.9%) which yield long effective absorption path lengths. In CEAS, light generated from a high intensity broad-band light source (e.g., a Xe arc lamp) is transmitted through an optical cavity set up in a stable resonator configuration. The output spectrum is integrated yielding extinction spectra from which mixing ratios are
35   retrieved using techniques analogous to those used in differential optical absorption spectroscopy (DOAS) (Platt and

Stutz, 2008). To date, CEAS has been used to quantify mixing ratios of many atmospherically important trace gases, including nitrogen dioxide (NO_2) (Langridge et al., 2008; Gherman et al., 2008; Triki et al., 2008; Thalman and Volkamer, 2010; Wu et al., 2014; Min et al., 2016), the nitrate radical (NO_3) (Langridge et al., 2008; Schuster et al., 2009), iodine (I_2), the iodine oxides IO and OIO (Vaughan et al., 2008), glyoxal (HCOHCO) (Washenfelder et al.,

40   2008; Thalman and Volkamer, 2010; Coburn et al., 2014; Min et al., 2016), methyl glyoxal (CH_3COCHO) (Thalman and Volkamer, 2010; Thalman et al., 2015; Min et al., 2016), molecular bromine (Br_2), bromine monoxide (BrO) (Chen and Venables, 2011; Hoch et al., 2014), formaldehyde (Washenfelder et al., 2016), and nitrous acid (HONO) (Gherman et al., 2008; Wu et al., 2014; Min et al., 2016).

The accuracy of retrievals depends on knowledge of relevant absorption and scattering (i.e., Rayleigh) cross-sections

45   (which both contribute to the optical extinction) and of the mirror reflectivity. Because of its high sensitivity, CEAS in turn has been utilized to measure these parameters. For example, Axson et al. and Kahan et al. recently reported the absorption cross-sections of O_3 and H_2O_2 (Axson et al., 2011; Kahan et al., 2012), and Thalman and Volkamer reported scattering cross-sections of N_2, O_2, Ar, and air (2010) for several wavelength intervals (345 – 390, 435 – 490, 515 – 545, 560 – 600, and 600 – 700 nm).

50   In spite of the large number of CEAS instruments that have been constructed, the mid-visible region has received relatively little attention to date, other than the pioneering study by Vaughan et al. (2008), even though the absorption maxima of several key atmospheric traces gases, such as NO_2 and the iodine species I_2, IO and OIO, are located in this wavelength interval (Figure 1). The study of iodine chemistry has been of considerable interest due to potential effects on the formation of new particles and atmospheric oxidising capacity through, for example, catalytic destruction of

55   O_3, altering the partitioning of NO_x (= NO + NO_2) and HO_x (= HO + HO_2), or the activation of chlorine and bromine from sea salt aerosol in the marine and polar boundary layer, near salt lakes and volcanoes, and in the stratosphere (Saiz-Lopez et al., 2012). Prior laboratory measurements by Vaughan et al. used a 150 W Xenon arc lamp; such light sources tend to flicker, i.e., exhibit intensity fluctuations, which add noise to the absorption spectrum. For this and other reasons (such as compactness, heat generation, etc.), light-emitting diodes (LEDs) are now commonly used to

60   generate broad-band radiation (Washenfelder et al., 2008; Min et al., 2016).

In this paper, we describe an LED-powered broadband CEAS operated in the cyan region of the electromagnetic spectrum. We report laboratory measurements of scattering cross-sections for N_2, O_2, Ar, CO_2, CH_4 and air from 480 to 535 nm and demonstrate detection of NO_2 and I_2 in laboratory-generated air. The CEAS was operated during the Ozone-depleting Reactions in a Coastal Atmosphere (ORCA) field campaign, conducted July 8-31, 2015 at the

65   Amphitrite Point Observatory (APO) in Ucluelet on the west coast of Vancouver Island, British Columbia (Tokarek et al., 2017). Kelp forests are present along this coast line (Watson and Estes, 2011), which are expected to emit I_2 (Dixneuf et al., 2009; Nitschke et al., 2015). Mixing ratios of NO_2 retrieved from the cyan CEAS data are compared to those measured by a co-located blue diode laser cavity ring-down spectrometer. The potential of the instrument for quantification of iodine species in laboratory and field experiments is assessed.

70

2 Theory

2.1 Cavity-enhanced spectroscopy

The principle of broadband trace gas measurements by CEAS has been described elsewhere (Fiedler et al., 2003; Washenfelder et al., 2008). Briefly, broadband radiation is continuously injected and trapped between a set of highly reflective mirrors forming a stable resonant cavity. The integrated cavity output intensity represents the combined extinction by the mirrors and the intra cavity medium. The absorption coefficient, $\alpha_{abs}(\lambda)$, is given in terms of the transmission signal through the cavity (Washenfelder et al., 2008) by Eq. (1):

$$\alpha_{abs}(\lambda) = R_L \left(\frac{1-R(\lambda)}{d} + \alpha_{Ray}(\lambda) \right) \left(\frac{I_0(\lambda)-I(\lambda)}{I(\lambda)} \right) \tag{1}$$

Here, R_L (see Sect. 3.3) is the ratio of the cell length ($d \approx 102$ cm) divided by the length occupied by the sample ($d_0 \approx 73$ cm), $R(\lambda)$ is the average wavelength dependent mirror reflectivity, d is the distance between the two reflective surfaces (i.e. the cavity length), $\alpha_{Ray}(\lambda)$ is the sum of all Rayleigh scattering sample constituents, $I_0(\lambda)$ is the intensity spectrum in the absence of absorbers in the cavity cell, and $I(\lambda)$ is the intensity spectrum measured in the presence of absorbers. When measurements are carried out in variable pressure environments (e.g., aircraft altitude change), an additional term ($\Delta\alpha_{Ray}(\lambda)$) is added to Eq. (1) to account for pressure fluctuations (Min et al., 2016). If multiple absorbers are present in the cavity, the absorption coefficient becomes the sum of all species expressed as in Eq. (2) (Washenfelder et al., 2008).

$$\alpha_{abs} = \sum_i^n \alpha_i(\lambda) = \sum_i^n N_i \, \sigma_i(\lambda, T, p) \tag{2}$$

Here, $\sigma_i(\lambda, T, p)$ is the wavelength, temperature, and pressure-dependent absorption cross-section, and N_i is the number density of the ith absorbing gas.

2.3 Determination of Rayleigh scattering cross-sections

Cavity-enhanced spectroscopic techniques allow accurate and precise measurements of Rayleigh scattering cross-sections of pure gases over broad wavelength regions (Naus and Ubachs, 2000; Sneep and Ubachs, 2005; Axson et al., 2011; Kahan et al., 2012; Thalman et al., 2014). If the mirror reflectivity $R(\lambda)$ is known, the scattering cross-section of any gas can be determined by measuring its extinction and that of a reference gas (Thalman et al., 2014), e.g., for CO_2 and using He as a reference:

$$\alpha_{Ray}^{CO_2}(\lambda) = \left(\left(\frac{1-R(\lambda)}{d} \right) \left(1 - \frac{I_{CO_2}(\lambda)}{I_{He}(\lambda)} \right) + \alpha_{Ray}^{He}(\lambda) \right) \left(\frac{I_{He}(\lambda)}{I_{CO_2}(\lambda)} \right) \tag{3}$$

Here, $\alpha_{Ray}(\lambda)$ is the optical extinction (in cm^{-1}) caused by the intra-cavity scattering medium. The scattering cross-sections are then calculated through division by the number density of the gas (N_{gas}), i.e.,

$$\sigma_{Ray}(\lambda) = \frac{\alpha_{Ray}(\lambda)}{N_{gas}} \tag{4}$$

100 Scattering cross-sections can be predicted if the refractive index, n, of a gas is known (Naus and Ubachs, 2000; Sneep and Ubachs, 2005), hereafter referred to as an "n-based" cross-section:

$$\sigma(\nu) = \frac{24\pi^3 \nu^4}{N^2} \left(\frac{n^2(\nu)-1}{n^2(\nu)+1} \right)^2 F_k(\nu) \tag{5}$$

Here, ν is the frequency in wavenumbers (cm^{-1}), $n(\nu)$ is the frequency dependent refractive index of the gas, and F_k is the King depolarization ratio which describes the effect of molecular anisotropy (King, 1923).

105 **3 Experimental**

3.1 Description of the CEAS instrument

The CEAS instrument consists of an LED light source, collimating optics, a high finesse resonant optical cavity, focusing optics, specialized fibre bundle, and a spectrograph equipped with a charge-coupled device (CCD) camera (Figure 2).

110 The resonant optical cavity consists of two dielectric-coated, plano-concave fused silica substrate mirrors (Advanced Thin Films, Boulder, CO, USA) with maximum reflectivity from 460 to 550 nm, 2.54 cm in diameter, 0.635 cm thickness, and 1 m radius of curvature. To span a broad wavelength range, the mirrors were coated with two highly reflective substrates, resulting in a double maximum in their reflectivity. The mirrors were mounted on both ends of a 102 cm long cell with a gas sampling region of ~73 cm and housed in a custom-built mount equipped with purge 115 gas ports. A flow of 50 standard cubic centimeters per minute (sccm) of ultrapure air ("zero" grade, Praxair) set using 50 μm critical orifices (Lenox Laser, Glen Arm, MD, USA) and a gas regulator back pressure of 20 pounds per square inch (psi; 1 psi = 6.9 kPa) was directed to each mirror to protect the optical surfaces from contamination. The mirror mounts were attached to adjustable kinematic mounts (Newport U200-A, Irvine, CA, USA) each equipped with 3 set screws for mirror alignment. The gas sampling region was enclosed using 1.9 cm outer diameter (o.d.) and 1.59 cm 120 inner diameter (i.d.) fluorinated ethylene propylene (FEP) Teflon™ tubing (Saint Gobain Plastics, Chemfluor series). The Teflon™ tube was held in place by a custom enclosure constructed from Aluminium. Gases entered and exited the sampling region through 1.9 cm o.d. perfluoroalkoxy alkane (PFA) Teflon™ fittings (Entegris Fluid Handling, Billerica, MA, USA).

The LED (Thorlabs M505L3, Newton, NJ, USA) output was collimated into the cavity by a single f/0.8 aspheric 125 condenser lens (Thorlabs ACL2520U-A). The cavity output was collected and focused by a 2.5 cm diameter f/1 lens through a non-polarizing quartz beam splitter (Thorlabs BS025) onto a 0.5 cm (diameter) f/4 fibre adapter that couples the radiation into a 2 m long 0.22 numerical aperture (NA) fibre bundle (Thorlabs BFL200HS02). The beam splitter has 90% transmission efficiency in the plane parallel to the cavity and 10% in the orthogonal plane and was used to direct the emission lines of a Hg(Ne) spectral calibration lamp (Newport Oriel 6032) towards the detector for 130 calibration of the spectrometer wavelength scale and line width. The fibre bundle consists of 7×200 μm optical fibres arranged with circular and linear configurations on the input and output, respectively. The fibre bundle output was oriented linearly along the spectrograph entrance slit to optimize coupling of the cavity output similar to (Min et al., 2016; Washenfelder et al., 2016), and illuminated the full vertical dimension of the CCD. Spectra were acquired by a

150 cm focal length f/4 dual grating Czerny-Turner spectrograph (Princeton Instruments Acton SP2156, Trenton, NJ,
USA) which back-illuminates a 16-bit 1340 × 100 pixel CCD array (Princeton Instruments, PIXIS 100B), mounted
at the focal plane of the spectrograph and Peltier-cooled to -80 ℃ to reduce thermal noise. The spectrograph was
configured with a 1200 groove mm^{-1} grating blazed at 500 nm. This configuration along with the grating positioned
at 500 nm central wavelength yielded spectral coverage from 446.9 to 563.2 nm spanning a total of 1340 discreet
wavelength points. The Acton SP2156 spectrograph shipped with a mechanical shutter, which was removed in lieu of
software control of the integration time via Labview™ (National Instruments, Austin TX, USA).

A fixed entrance slit width of 50 μm yielded an approximately Gaussian profile with full-width at half maximum
(FWHM) of (0.330±0.003) nm at 540.06 nm. Other spectral lines (e.g., 520.39 nm) showed slightly degraded
resolution of roughly (0.360±0.016) nm (Figure S1). An integration time of 5-6 s saturated the CCD pixels 80–90%
of their well depth near 500 nm.

All mechanical and optical components were mounted on an optical breadboard (Thorlabs MB2448) bolted onto
aluminium structural rails (80/20, Columbia City, IN, USA). The net instrument weight including the breadboard and
railing is < 90 kg and the overall power consumption below 300 W.

The CEAS samples air through a 47 mm diameter, circular, permeable polytetrafluoroethylene (PTFE) Teflon™
membrane filter with 1 μm pore size (Pall Teflon™ Series, Port Washington, NY, USA) housed in a PFA Teflon™
filter holder (Cole-Parmer R-06621-40) and through 0.635 cm outer diameter and 0.476 cm FEP Teflon™ tubing. The
sample flow was set using a mass flow controller (MFC, MKS Instruments 100 B series, 15 standard litres per minute
(slpm) capacity, Andover, MA, USA) connected to a diaphragm pump (KNF Neuberger UNO26.1.2ATP, Trenton,
NJ, USA). The sample flow was in the range 1.5–2.5 slpm resulting in a sample residence time of 5.9–3.5 s. The gas
temperature was measured using a K-type thermocouple (Omega, Laval, QC, Canada) attached to the aluminium
sample cell enclosure. Pressure was measured using a pressure transducer (MKS Baratron capacitance manometer
722B) mounted on the exhaust portion of the CEAS between the gas sample cell and the MFC.

The light source is a small footprint (1×1 mm) broadband LED (M505L3, Thorlabs) mounted on the end of a heat
sink supplied by the manufacturer. We modified this assembly by mounting a Peltier module (CUI Inc. CP30238,
Tualatin, Oregon, USA) between the LED and the heat sink for temperature control using a proportional–integral–
derivative (PID) controller (Omega CNi3253) to 30.0±0.1 ℃. If not stabilized, the LED output red-shifted ~0.1 nm
per °C temperature change. The LED was operated just below the maximum current of 1000 mA (3.3 W of electrical
power) to achieve a manufacturer quoted optical minimum output power of ~400 mW.

The LED output spectrum was characterized by an asymmetric Lorentzian shape, an emission maximum at 507.5 nm,
and a peak width of 22.5 nm FWHM, and was a good match with the mirror reflectivity curve (Figure 3).

3.2 Determination of the mirror reflectivity

The response of the CEAS instrument depends on $R(\lambda)$ and d_0 (Eq. (1)), which need to be accurately known. If an
optical cavity is filled with a non-absorbing and inert gas, and aerosol are removed by filtering, the optical extinction
is due to gas scattering only. In this case, $R(\lambda)$ can be derived from the extinction caused by two individual gases with
known and different scattering cross-sections such as N_2 and He (Washenfelder et al., 2008):

170
$$R(\lambda) = 1 - d \frac{\alpha_{Ray}^{N_2}(\lambda)\frac{I_{N_2}(\lambda)}{I_{He}(\lambda)} - \alpha_{Ray}^{He}(\lambda)}{1 - \frac{I_{N_2}(\lambda)}{I_{He}(\lambda)}}$$ (6)

Here, $I_X(\lambda)$ and $\alpha_{Ray}^X(\lambda)$ are the intensities and extinction coefficients of N_2 and He, respectively, and d is in units of cm. Other pairs (e.g., He and Ar) may be used as well. For this work, we chose scattering cross-sections from (Peck and Khanna, 1966) for N_2, (Cuthbertson and Cuthbertson, 1932) for He, and (Peck and Fisher, 1964) for Ar. Typically, combinations with He provide a higher signal-to-noise due to He having a much smaller scattering cross-section than other gases (Thalman et al., 2014). The above approach assumes that scattering and absorption within the optical cavity are small (Washenfelder et al., 2008) and neglects absorption and scattering due to the mirror substrate.

To determine $R(\lambda)$ in this work, the cavity output intensity was recorded when the cell was filled with high purity N_2 (99.998%) or with He (99.998%) to atmospheric pressure. In each case, the gases were continuously injected through the purge ports until all other sample cell constituents were displaced through the open inlet port. To corroborate the results, the cavity was also filled with Ar (99.998%), which has slightly larger scattering cross-sections than that of N_2.

Figure 3a shows cavity-enhanced transmission spectra with the optical cavity filled with N_2, He, and Ar, each averaged over a 15 min time period. The intensity difference due to scattering by Ar and N_2 was more pronounced in the case when the sample cell was filled with He (Figure 3a, inset), as expected based on their relative cross-sections (Thalman et al., 2014).

Figure 3b shows the reflectivity spectra calculated using Eq. (6). The reflectivity curves are essentially smooth continua, with maximum reflectivity of ~99.98%. The relative difference between the reflectivity calculated from the ratios of Ar/He and N_2/He was $< 1.6 \times 10^{-6}$ in the 480–530 nm range. Arbitrarily, the N_2/He mirror curve was chosen to calculate the mirror reflectivity for the remaining data analysis in this work with the exception of the scattering cross-sections of N_2 and CO_2 (see Sect. 4.1.1 and 4.1.5) for which the Ar/He pair was used. The observed reflectivity corresponds to a total path length ($\approx d/(1-R)$) of 5.5 and 6.3 km near 485 nm and 520 nm, respectively. Intermittent measurements of mirror reflectivity showed that it remained unchanged throughout this work; in particular, no difference in reflectivity was found prior to and following the ORCA campaign.

The overall uncertainty in the measured mirror reflectivity was ±2.3%, resulting from addition by quadrature of a ±1% uncertainty in the N_2 scattering cross-section (Peck and Khanna, 1966), a ±2% uncertainty in the He cross-section (Washenfelder et al., 2008; Min et al., 2016), ±0.4% uncertainty in temperature, ±0.1% uncertainty in pressure, and ±0.1% random noise due to photon counting statistics.

3.3 Determination of the effective optical absorption path

Knowledge of the path length over which sampled air is present (d_0) is essential in experiments involving resonant optical cavities, especially when purging gases are used to maintain clean mirrors as in this work. If the mirror reflectivity R is known, d_0 can be determined by measuring the extinction of a known amount of a strongly absorbing, non-reactive gas with known absorption cross-section, which is sampled through the inlet port. Combining Eq. (1) and Eq. (2) and rearranging gives an expression for d_0:

$$d_0 = \frac{\delta I(\lambda)}{\sigma N} \left(1 - R(\lambda) + d\alpha_{Ray}(\lambda)\right) \tag{7}$$

Here, $\delta I(\lambda) = [I_0(\lambda) - I(\lambda)]/I(\lambda)$. In this work, we used water vapour and the absorption cross-section of H_2O from (Coheur et al., 2002) to determine $R_L = d/d_0$. A saturated gas stream of water vapour was generated by bubbling air through a water reservoir at a temperature of 298 K and pressure of 0.88 atm. Using Eq. (4), d_0 was found to be 73.2±0.7 cm, in agreement with the physical dimension (~73 cm) of the CEAS sample path. With $d = 102.0$ cm, this gives $R_L = 1.39\pm0.01$.

3.4 Reference absorption cross-sections

Figure 1 shows trace absorbers in the 480–530 nm window calculated as extinction ($\alpha_i(\lambda) = \sigma_i(\lambda)N$) for typical atmospheric mixing ratios. CEAS analysis was performed using the high-resolution NO_2 absorption cross-section of Voigt et al. (2002) and the cross-sections of Spietz et al. for OIO (2005) and I_2 (2006), respectively. The NO_2 cross-section was convolved with the instrument function corresponding to a sharp peak line (540.06 nm) in the emission spectrum of the Hg(Ne) calibration lamp (Figure S2), which was also used to calibrate the wavelength scale of the spectrometer.

The CEAS spectrometer resolution was 0.33 nm in the 480–530 nm window, whereas the NO_2 literature spectrum was recorded at a higher resolution of better than 0.005 nm (Voigt et al., 2002). Convolving the NO_2 reference spectrum effectively degraded the high-resolution spectrum but was required for the least-squares analysis. The literature cross-sections of I_2 and OIO (2005; 2006) were not convolved because their resolution was lower than that of the CEAS.

The NO_2 absorption cross-section is somewhat pressure-dependent, which is important considering that the CEAS was operated at ~350 Torr in the field. Voigt et al. (2002) reported cross-sections at 1000 and 100 Torr (in N_2). Following convolution to the (relatively) low resolution CEAS instrument, these differences were judged to be small (2 – 5% in the 480 – 530 nm range).

3.5 Spectral fitting

The DOAS intelligent system (DOASIS; (Kraus, 2003)) was used to retrieve gas-phase concentrations. Optical extinction data collected in laboratory experiments were fitted using the literature absorption spectra (Sect. 3.3) and a third-degree polynomial to represent broad-band processes (e.g., temperature fluctuation, Mie scattering and extinction by aerosols). The "spectral shifting" setting in DOASIS was set to ±0.2 nm, and stretching was disallowed. The contributions of water vapor to the optical extinction was neglected since the relative humidity of the air sampled during the background measurement was the same as during the measurement of NO_2 or I_2.

The same parameters were used to fit the data from the ORCA field campaign except that in an effort to minimize the fit residuals, the absorption cross-section of H_2O (Coheur et al., 2002) was also included in the fit. Further, the optical extinction (α) values, as per Eq. (1), were smoothed using a fourth order polynomial filter (Savitzky and Golay, 1964).

Smoothing improved the root mean square (RMS) of the residuals and the fit uncertainty by a factor of ~2 (Figure
S3).

3.6 Description of CRDS instrument

The CEAS instrument quantified NO_2 in parallel to a blue diode laser CRDS, which has been described previously
240   (Paul and Osthoff, 2010; Odame-Ankrah, 2015). Briefly, mixing ratios of NO_2 are quantified by optical absorption
using a continuous wave (cw) laser whose emission is centered at 405 nm (Power Technology IQμ2A105, Little Rock,
AR, USA). The radiation is square-wave (on/off) modulated at a repetition rate of 1 kHz (50% duty cycle) and enters
a 111 cm long stable resonator formed by two highly reflective mirrors (2.54 cm diameter; Advanced Thin Films,
Boulder, CO, USA) in a concentric configuration. The cavity output is coupled into a 200 μm diameter, 0.22 numerical
245   aperture, multimode optical fibre (Thorlabs M25L01) illuminating a photomultiplier tube (Hamamatsu Photonics
H9433-03MOD, Japan). The ring-down decay traces are co-added and fitted to an exponential using the discrete sums
algorithm described by Everest and Atkinson (2008).

The CRDS NO_2 channel was operated in parallel to a CRDS NO_x channel, to which a small flow of O_3 in O_2 was
added to convert NO to NO_2, similar to the method described by Fuchs et al. (2009). Following the O_3 addition point,
250   the sampled air passed through a coiled reaction chamber with a total residence time of ~7 s to ensure complete titration
and a linear response up to ~100 ppbv of NO (Odame-Ankrah, 2015). An identical chamber was added to the NO_2
channel to match the response times of the two channels. Mixing ratios of NO_2 and NO_x measured by CRDS were
accurate within ±10% (Osthoff et al., 2017).

3.7 Generation and delivery of calibration gases

255   Figure 2b shows the setup for delivery and sampling of NO_2. NO_2 was generated by mixing the output of a standard
NO cylinder (100.2±1.0 ppmv in N_2; Scott-Marrin, Riverside, CA, USA) delivered using a 20 sccm all metal MFC
(MKS Instruments 1479A) with O_3 produced by illuminating a flow of O_2 (Praxair) with a 254 nm Hg pen-ray lamp
(Jelight, Irvine, CA, USA) and dilution with zero air.

Iodine was purchased in a solid crystalline form (≥99.8%, Sigma-Aldrich, Oakville, ON, Canada). Small amounts
260   were placed in a Teflon™ permeation tube (VICI Metronics, Poulsbo, WA, USA); these tubes were sealed on both
ends with PTFE plugs compressed with stainless steel rings and were (individually) placed in a temperature-controlled
permeation chamber (Vici Metronics, model 120-1) operated with a constant air flow of ~0.3 litres per minute. The
flow from the permeation chamber was diluted with zero air, yielding iodine concentrations in the range of ~70 pptv
up to 21 ppbv depending on chamber temperature and permeation tube dimensions (i.e., wall thickness and length).

3.8 ORCA field campaign

The CEAS was operated alongside the CRDS during a four week long field intensive conducted at the Amphitrite
Point Observatory (APO) on the west coast of Vancouver Island, British Columbia, Canada (Tokarek et al., 2017).

The APO was established as a marine background monitoring site but is sporadically impacted by NO_x emissions mainly from ship and boat traffic in the region (McKendry et al., 2014).

270   The CEAS and CRDS sampled, in parallel, from a 5.5 m long common 0.63 cm o.d. and 0.48 cm i.d. FEP Teflon™ inlet line, flooded with calibration gases and zero air in regular intervals. Zero air was generated using a custom-built zero air generation system (Odame-Ankrah, 2015), which delivered air at ambient relative humidity that was free of trace gases such as NO_2, NO, I_2, or O_3. A flow restriction was placed upstream of the inlet filter. When the CEAS was operated at a flow rate of 5 slpm, an average ($\pm 1\sigma$) sample cell pressure of 355 (± 17) Torr and inlet residence time of

275   2.3 s were achieved. The cell pressure varied over short time periods with a standard deviation of ± 1.8 Torr.

The CEAS transmission spectrum was integrated for 9 s, resulting in ~90% saturation of the CCD at 500 nm. Dark spectra (to characterize the spectrometer offset) were acquired daily with the same integration time (9 s). Wavelength calibration spectra of the Hg(Ne) lamp were collected daily over a period of 2 min and showed that the spectrometer wavelength scale remained relatively unchanged (± 0.02 nm) over the region of interest. The mirror reflectivity was

280   measured prior to and after the campaign and agreed within $\pm(1 \times 10^{-7})$. Data were averaged over 60 s post-campaign prior to analysis.

4 Results

4.1 Measurements of cross-sections of pure gases

285   The extinction cross-sections of N_2, CO_2 (based on mirror reflectivity determined from the Ar/He ratio of scattering coefficients) O_2, air, Ar, and CH_4 (based on mirror reflectivity determined from the N_2/He ratio of scattering coefficients) in the 480–535 nm wavelength range are shown in Figure 4; values at selected wavelengths are summarized in Table 1. For N_2, Ar, and CO_2, the extinction is due to scattering only. In contrast, the spectra of O_2, air and CH_4 include optical losses due to absorption in addition to scattering. The systematic uncertainty of these data

290   was $\pm 2.5\%$; the systematic errors arise mainly from uncertainties in the mirror reflectivity ($\pm 2.3\%$, see Sect. 3.2) and errors in the scattering cross-section terms in Eq. (3). The precision of the data (calculated after subtracting a 4th order polynomial from the observed cross-sections) varies from $\pm 2.5\%$ for the CO_2 data shown in Figure 4e to $\pm 0.9\%$ for the N_2 data shown in Figure 4b.

4.1.1 Nitrogen

295   Figure 4b shows the measured scattering cross-sections of N_2 at a temperature of 299.0 ± 0.1 K and pressure of 660.0 ± 0.5 Torr between 480 and 535 nm. Superimposed are n-based cross-sections predicted using Eq. (5), data by (Peck and Khanna, 1966), and the King correction factor by (Bates, 1984). In addition, the single wavelength CRDS measurement at 532.2 nm by (Sneep and Ubachs, 2005) and the nephelometer data of (Shardanand and Rao, 1977) are shown.

300   The CEAS data are marginally larger than the n-based prediction, with the percent difference ranging from +0.2% at 525.07 nm to +1.3% at 485.03 nm (Table 1). These differences are well within the margin of measurement error

(±2.5%), set in this case by the accuracy of the scattering cross-sections of He (±2%) and Ar (<1%). The CEAS data differ from the CRDS data of (Sneep and Ubachs, 2005) at 532.2 nm by +7.1%, though the error bars overlap; the measurement uncertainty of the CRDS data alone is ±9.4%. The CEAS measurements also differ by +4.6% at 488.0

305   nm and by +8.8% at 514.5 nm) from the data of (Shardanand and Rao, 1977) but are within combined measurement error (±2.5% and ±11%, respectively).

4.1.2 Argon

The scattering cross-sections of Ar at 299.0±0.1 K and 660.0±0.5 Torr are shown in Figure 4b. Superimposed are the n-based cross-sections calculated using data from (Peck and Fisher, 1964) and the King correction factor from (Bates,

310   1984). The single-wavelength measurement of (Sneep and Ubachs, 2005) and the nephelometer data of (Shardanand and Rao, 1977) are shown for comparison.

The observed scattering cross-sections are marginally larger than the n-based prediction, by +1.3% at shorter wavelengths and +0.21% at 515.06 nm (Table 1). These differences are within measurement error of the CEAS (±2.5%) inferred from the accuracy in the determination of the scattering cross-sections of He (±2%) and N_2 (±1%)

315   used in the determination of the mirror reflectivity. The CEAS cross-sections differ from the CRDS data by (Sneep and Ubachs, 2005) at 532.2 nm and are well within either measurement error bar (Figure 4b). In contrast, the CEAS values differ from the nephelometer data by -10.8% at 488.0 nm and by -5.1% at 514.5 nm, though they are within the ±11% uncertainty of the nephelometer.

4.1.3 Oxygen

320   The extinction cross-sections of O_2 (at a temperature of 299 K and a pressure of 660 Torr) are shown in Figure 4c next to the n-based predictions based on (Bates, 1984) and the nephelometer measurements of (Shardanand and Rao, 1977). The CEAS data show two absorption bands due to the oxygen dimer, O_4, centered at 477 nm and 532 nm (Thalman and Volkamer, 2013). In the 490 – 515 nm wavelength interval, the contribution of these absorption bands to the total extinction is negligible (<0.2% at 515 nm), i.e., the extinction is dominated by scattering. In this region, the observed

325   cross-sections are slightly larger than the n-based data of (Bates, 1984): the differences range from +8.3% at 495.08 nm to +2.5% at 515.06 nm (Table 1). Relative to the nephelometer measurements, the CEAS data differ by +8.7% at 488 nm and by +15.3% at 514.5 nm.

We calculated the absorption cross-section of O_4 by subtracting the scattering cross-section of (Bates, 1984), upshifted by +3.86×10^{-28} cm^2 molecule^{-1} (i.e., by 6%) to match the n-based data to the observed extinction from 487 nm to

330   516 nm, from the extinction shown in Figure 4c, and dividing by the number density of O_2 (2.13×10^{19} molecules cm^{-3}). The result is shown in Figure S4. The error for this absorption cross-section calculation is estimated at ±8.5%, with the largest source of error being the correction to the scattering cross-section extrapolated from the region where absorption is negligible, For the smaller band between 520 and 540 nm, the observed cross-section of (1.08±0.09)×10^{-46} cm^5 molecule^{-2} is in agreement with recent room-temperature measurements by other groups (Table S1). For the

335   larger band between 467 and 485 nm, the peak cross-section of (6.2±0.5)×10^{-46} cm^5 molecule^{-2} is smaller than that

reported in recent measurements (Thalman and Volkamer, 2013; Sneep et al., 2006), though the shape of the peak is identical and the error bars overlap.

4.1.4 Air

Figure 4d shows the extinction spectrum of ultrapure air ("zero" grade, Praxair) at a temperature of (298.5±0.1) K and
340   pressure of (660.5±0.5) Torr. Superimposed is the *n*-based prediction from the refractive index data of (Penndorf, 1957) and King correction factor from (Bodhaine et al., 1999).

The sample cylinder contains a sufficiently high quantity of O_2 (~19.5% by volume, Praxair) for O_4 absorption bands to appear at 477.5 and 531.5 nm. In the 495 - 515 nm wavelength region, the cross-sections observed by CEAS are slightly larger than the *n*-based prediction, by +4.0%, +3.0%, and +6.8% at 495, 505, and 515 nm, respectively (Table
345   1).

4.1.5 Carbon dioxide

Figure 4e shows the scattering cross-sections of CO_2 at (299.0±0.1) K and (660.0±0.5) Torr for the 475 – 540 nm wavelength interval. Superimposed are the *n*-based prediction based on (1973), nephelometer measurements (1977), and a CRDS measurement at 532.2 nm (2005). The observed scattering cross-sections differ from the *n*-based
350   prediction by -2.9%, +2.4% and -2.8% at 485 nm, 505 nm, and 525 nm, respectively (Table 1). In contrast, the CRDS measurement at 532.2 nm, which has a relatively high uncertainty of ±6.5% at the 1σ level, is 11% lower than the CEAS measurement. The nephelometer measurements (1977), on the other hand, are significantly larger than the other data shown and appear to be in error.

4.1.6 Methane

355   Figure 4f shows the extinction spectrum of CH_4 (research grade, 99.97%) for the 475 – 550 nm interval at (298.5±0.1) K and (660.5±0.5) Torr. The CH_4 spectrum in this region contains a number of combination and overtone absorption bands near 484.7, 486.1, 509.6, 522.0, and 543.4 nm that have been assigned by (Giver, 1978). These bands are relevant to studies simulating the atmospheres of Jovian planets (e.g., Uranus, Neptune) and Saturn's moon Titan that contain CH_4 (Karkoschka, 1994). Superimposed are CRDS data by (Sneep and Ubachs, 2005) and the *n*-based
360   scattering cross-sections, calculated using the parameterization by Sneep and Ubachs, and refractive index data from (Hohm, 1993), assuming a depolarization ratio of unity and nephelometer data by (Shardanand and Rao, 1977) extrapolated using Eq. (5) (dashed line). In spite of the many absorption bands, there are small windows where the optical extinction appears to be dominated by scattering and a comparison with literature is feasible. There is very little difference (within combined measurement errors) between CEAS and interpolated nephelometer data at those
365   wavelengths. At 492.06 nm and 527.28 nm, for example, the data are within -0.07% and 0.17%, respectively (Table 1). There is also reasonable agreement between the CEAS and CRDS data 532.2 nm, which differ by 4.7% but compares well with the total CEAS uncertainty of 4.6% for CH_4.

4.2 Measurement of trace gas mixing ratios

4.2.1 Nitrogen dioxide

370 An example NO_2 CEAS measurement is shown on Figure 5a. The figure shows the measured optical extinction (α) for a routine calibration period during the ORCA campaign on 22 Jul, 2015 at 11:52:07 to 11:57:02 (UTC). Superimposed is a fit determined with DOASIS. An NO_2 mixing ratio of (11.6 ± 0.4) ppbv was retrieved. The residual spectrum is lacking structure, indicating that other absorbers are not significant in this wavelength region.

During the ORCA campaign, the inlet of the CEAS (and CRDS, which sampled in parallel) was overflowed every 30
375 min with a standard gas mixture of ~20 ppbv NO_x containing up to 16 ppbv of NO_2 in zero air and with ~130 ppbv of NO added to ambient air. The zero air was generated using a scrubber constructed in-house that delivered air with a similar moisture content as ambient air. A subset of these data (and the ambient air data sampled in between) is shown in Figure 6a.

High concentrations of NO in air are prone to oxidation (by O_3 and, to a lesser degree, by O_2) to NO_2 (Atkinson et al.,
380 2004). Because the CRDS had a longer inlet residence time (7 s) than the CEAS (2.3 s), it observed greater conversion of NO to NO_2 when the high NO concentration standard was sampled in an ambient air matrix. On the other hand, when the lower concentration NO_x standard was sampled in O_3-free air, the two instruments agreed well (Figure 6a). Shown in Figure 7a is a scatter plot of all of the NO_x calibration data. This plot shows a linear relationship with a slope of 0.923 ± 0.009, an intercept of 0.18 ± 0.09 ppbv, and $r^2 = 0.975$. The slope of the line in Figure 7a reveals 7.7%
385 difference in measurement of the calibration standard.

In ambient air, the median NO_2 mixing ratio during ORCA was 1.24 ppbv. Shown in Figure 6b is a time series of a subset of ambient air NO_2 measurements. The CEAS NO_2 data clearly exhibit more scatter than the CRDS NO_2 data and occasionally fall below zero. The scatter plot of CEAS and CRDS NO_2 data (Figures 7b and 7c) suggest that the CRDS data were systematically higher than the CEAS data, by 15% when sampling ambient air (Figure 7c). When
390 data are filtered by removing all CEAS points below a factor of three times the standard deviation of a blank measurement for 60 s (~1 ppbv; see Sect. 4.3), the slope of the scatter plot, when forced through an intercept of zero, is 0.98 ± 0.01 ($r^2 = 0.070$).

4.2.2 Molecular iodine

Figure 5b shows an example of an I_2 measurement. The extinction spectrum was recorded during the ORCA campaign
395 on 18 Jul 2015, when I_2 from a permeation source had been added to the inlet and represents a 60 s average. A mixing ratio of (10.1 ± 0.2) ppbv was retrieved in this example.

Figure S5 shows spectra of laboratory generated I_2 samples and their respective absorption spectra, fits, and residuals. The smallest amount of I_2 that was produce without dilution of the permeation chamber output flow was ~21 pptv. Fit results near 20 pptv showed large residuals ($\pm 27\%$) indicating that the CEAS was near its detection limit.

400 A sample time series of laboratory I_2 measurements (30 s averaged data) is shown in Figure S6. Gas streams containing I_2 were generated using four permeation tubes of different wall thickness, that were exchanged while the output of the permeation was bypassed and the CEAS sampled zero air. The CEAS responded rapidly to concentration changes: for

example, at 22:05, the response 30 s after "zeroing" was 10% of the preceding value, indicating that memory effects (from slow adsorption / desorption kinetics of iodine on the inner walls of the inlet) were negligible. Figure S7 shows
405   a sample time series of I_2 mixing ratios during the ORCA campaign. Concentrations of I_2 in ambient air were below the instrument's detection limit. At 22:30 UTC, I_2 from a diffusion source was added to the inlet. The square-wave response and quick rise and fall times suggest the absence of inlet transmission losses.

4.3 Accuracy and limits of detection

The accuracy of the CEAS NO_2 measurement is influenced by uncertainties in the absorption cross-section of NO_2
410   (3%) (Voigt et al., 2002), fit errors (3 – 5%), which can be reduced to 2 – 4% by smoothing, scattering cross-sections (2.5%) (see Sect. 3.2 and 4.1), and calibration errors in the mass flow controller reading (1%), sample cell pressure readout (0.5%), and temperature measurement (0.7%). The total uncertainty, expressed as the square root of the individual errors summed in quadrature, is ±(5.5 – 7.6)%.

The limits of detection (LOD) were assessed through Allan deviation analyses (Werle et al., 1993). For NO_2 sampled
415   at a flow of 1.5 slpm and cell pressure of 668 Torr, the Allan deviation was ±278 pptv for 10 s data, 105 pptv for 60 s data, 49 pptv for 5 min data averages (Figure 8a). At the higher sample flow of 5 slpm and reduced cell pressure of 350 Torr used during the ORCA campaign, the Allen deviation was ±137 pptv for 334 s data (Figure S8).

For I_2 in laboratory-generated samples under optimal conditions, typical 1σ fit errors (when integrated over 60 s) were ±5.8 pptv for 21 pptv I_2 and ±7 pptv for 350 pptv I_2 (Figure S6). The accuracy for I_2 was (5.4 – 6.4)%, with main
420   contribution from error in the high-resolution absorption cross-section of I_2 (Spietz et al., 2006). The Allan deviation plot in Figure 8b demonstrates 1σ measurement precisions for I_2 of ±38 pptv for 60 s and ±16 pptv for 5 min averaged data. During ORCA, the 1σ precisions were ±100 pptv for 60 s and ±50 pptv, respectively.

For OIO, the Allan deviation analysis gives 1σ measurement precisions of ±4.6 pptv for 60 s and ±1.8 pptv for 5 min averaged data (Figure S9) in the laboratory.

425   **5 Discussion**

The CEAS described in this work adds to a growing number of instruments designed for measurement of atmospheric trace gases (Table 2). It differentiates itself foremost through its unique wavelength region, where several trace gases of atmospheric interest (e.g., NO_2, I_2, IO, OIO) absorb (Figure 1). Measurements of optical absorption in the cyan region enable simultaneous quantification of I_2, IO, and OIO in a single channel. Currently, such measurements require
430   multiple detection channels, for example quantification of I_2 and OIO mixing ratios using the 525 – 555 nm range and those of IO the 420 – 460 nm window in a separate channel (Vaughan et al., 2008). A reduction of channels and LEDs corresponds to savings in space and power requirements, important considerations in the field.

As such, this paper has laid some of the ground work for future measurements in the cyan spectral region, in that we measured relevant scattering and absorption cross-sections of pure gases (see S.I.). Such information is needed to
435   determine mirror reflectivity and is useful to probe the consistency of scattering cross-sections reported for this

wavelength region (of which there have been relatively few) and, hopefully, improve upon their accuracy, to better describe transmission of radiation through the atmosphere.

Scattering cross-section measurements for non-absorbing gases agree with all recent literature values (Figure 4 and Table 1). For example, the CEAS scattering cross-section measurements agree, within the combined experimental

440 uncertainties (1σ), with the CRDS data by (Sneep and Ubachs, 2005) at 532.2 nm for N_2, Ar, CO_2, and CH_4, and with the nephelometer measurements of (Shardanand and Rao, 1977) at 488.0 and 514.5 nm for N_2, Ar, O_2, and CH_4. For CO_2, the CEAS data closely match the data by Bideau-Mehu et al. (1973) and recent data by (He et al., 2018); the older data by (Shardanand and Rao, 1977), in contrast, appear high (Figure 4e).

In the case of CH_4, to lesser extent, O_2 and, air, the analysis is complicated by absorption lines. For O_2, our data and

445 derived collisional-induced absorption cross-sections agree with literature (Table S1). For regions that appear to be free of absorption bands, the CEAS data for CH_4 (Figure 4f) agree with cross-section measurements of (Shardanand and Rao, 1977) but not with the more recent work of (Hohm, 1993) whose data appear high. The CRDS data point by (Sneep and Ubachs, 2005) is on a shoulder of a large absorption band and hence not a valid measurement of scattering but extinction cross-section; their data agrees with the extinction cross-section observed in this work. Accurate

450 knowledge of the scattering cross-section of CH_4 is important to the study of planetary bodies with atmospheric content of CH_4 such as Saturn's moon Titan. Future studies should re-examine the scattering cross-section measurements of CH_4 to resolve the reported differences.

The detection limit for NO_2 achieved under laboratory conditions in this work (49 pptv for 5 min data) is compared to instruments operated in other wavelength regions (Table 2). However, the CEAS measurement precision in this work

455 was surpassed by the more mature blue diode CRDS, though future upgrades (e.g., more highly reflective mirrors, more sensitive spectrometer, etc.) may improve the CEAS precision. On the other hand, the CEAS may ultimately be more accurate. Unlike CEAS where all absorbing molecules are incorporated in the fit, the measurement of NO_2 by blue diode laser CRDS is prone to potential interference from molecules that absorb at 405 nm such as glyoxal and methyl glyoxal (Fuchs et al., 2009). For example, Fuchs et al. estimated that the presence of glyoxal could introduce

460 an interference of ~1% in polluted and up to 10% in forested environments (Fuchs et al., 2009). The low precision of the data in the scatter plot shown in Figure 7c prevents us from drawing a definitive conclusion as to the magnitude of such interferences. Still, future comparisons of CEAS and blue diode CRDS measurements of ambient NO_2 should be conducted. The data presented in this manuscript show that accurate measurements of NO_2 in ambient air by a cyan CEAS are possible.

465 The sensitivity for I_2 and OIO (16 and 1.8 pptv for 5 min averaged data under laboratory conditions) suffices for their quantification in environmental chamber studies (Dixneuf et al., 2009). Further, these LODs are below maximum I_2 and OIO abundances reported at Mace Head, Ireland, of 94 and 13 pptv (Bitter et al., 2005) and 61 and 9.2 pptv (Peters et al., 2005), respectively, but above the maximum I_2 level of 4 pptv reported in California (Finley and Saltzman, 2008). This implies that iodine species on the West coast of British Columbia, Canada, might have been detected if

470 the instrument had been operated optimally. Even then, the LOD for I_2 of 76 pptv (2σ, 60 s average) is larger than the LOD of 26 pptv (2σ, 60 s average) reported by Vaughan et al. (2008). This suggests that improvements are possible.

Below we discuss potential instrument modifications to improve the detection limit and sampling of iodine species in future field deployments.

One area for improvement is the thermal management of the LED. Its intensity and wavelength drifts with temperature, necessitating temperature stabilization to achieve a constant emission profile. In this work, the cyan LED was stabilized by mounting a single Peltier thermoelectric module and thermocouple between the heat sink and the LED. When evaluated in the climate-controlled laboratory, this yielded a cavity emission profile that varied along the entire wavelength range (446.9–563.2 nm) of the spectrometer by ± 15 counts (Figure S10). At 500 nm, this corresponded to an absorption coefficient of $\pm 1 \times 10^{-9}$ cm^{-1}. During the field deployment, however, the LED was subject to greater output fluctuations, since the trailer temperature was not as well controlled as in the laboratory, and thermal gradients between the LED and thermocouple may have come into play.

When deployed in the field, the performance of the CEAS was also compromised by variable cell pressure which added noise to the optical extinction, caused in part by the large pressure drop from ~760 to ~350 Torr. Furthermore, we discovered post-campaign that the alignment of the round-to-linear fiber bundle is very sensitive to vibrations, which would have added additional noise during the field campaign. In future deployments, improved pressure, temperature and vibrational stabilization of the sample cell (as it is common in aircraft deployments, for example) and instrument will be paramount.

Acknowledgments

This work was made possible by the financial support of the Natural Science and Engineering Research Council of Canada (NSERC) in the form of a Discovery grant, of the Canadian Foundation for Innovation (CFI) in the form of a LOF grant, and by the Government of Alberta's Advanced Education and Technology (AET) Small Equipment Grants Program (SEGP). The authors thank the Birrs and Thurbide groups at the University of Calgary for loans of CH_4 and CO_2 compressed gas cylinders used in this work.

References

Atkinson, R., Baulch, D. L., Cox, R. A., Crowley, J. N., Hampson, R. F., Hynes, R. G., Jenkin, M. E., Rossi, M. J., and Troe, J.: Evaluated kinetic and photochemical data for atmospheric chemistry: Volume I - gas phase reactions of O_x, HO_x, NO_x and SO_x species, Atmos. Chem. Phys., 4, 1461-1738, 10.5194/acp-4-1461-2004, 2004.

Axson, J. L., Washenfelder, R. A., Kahan, T. F., Young, C. J., Vaida, V., and Brown, S. S.: Absolute ozone absorption cross section in the Huggins Chappuis minimum (350 - 470 nm) at 296 K, Atmos. Chem. Phys., 11, 11581-11590, 10.5194/acp-11-11581-2011, 2011.

Bates, D. R.: Rayleigh scattering by air, Planetary and Space Science, 32, 785-790, 10.1016/0032-0633(84)90102-8, 1984.

Bideau-Mehu, A., Guern, Y., Abjean, R., and Johannin-Gilles, A.: Interferometric determination of the refractive index of carbon dioxide in the ultraviolet region, Optics Communications, 9, 432-434, 10.1016/0030-4018(73)90289-7, 1973.

Bitter, M., Ball, S. M., Povey, I. M., and Jones, R. L.: A broadband cavity ringdown spectrometer for in-situ measurements of atmospheric trace gases, Atmos. Chem. Phys., 5, 2547-2560, 10.5194/acp-5-2547-2005, 2005.

Bluvshtein, N., Flores, J. M., Riziq, A. A., and Rudich, Y.: An Approach for Faster Retrieval of Aerosols' Complex Refractive Index Using Cavity Ring-Down Spectroscopy, Aerosol Sci. Technol., 46, 1140-1150, 10.1080/02786826.2012.700141, 2012.

Bodhaine, B. A., Wood, N. B., Dutton, E. G., and Slusser, J. R.: On Rayleigh optical depth calculations, Journal of Atmospheric and Oceanic Technology, 16, 1854-1861, 10.1175/1520-0426(1999)016<1854:ORODC>2.0.CO;2, 1999.

Burkholder, J. B., and Talukdar, R. K.: Temperature-Dependence of the Ozone Absorption-Spectrum over the Wavelength Range 410 to 760 nm, Geophys. Res. Lett., 21, 581-584, 10.1029/93GL02311, 1994.

Chen, J., and Venables, D. S.: A broadband optical cavity spectrometer for measuring weak near-ultraviolet absorption spectra of gases, Atmos. Meas. Tech., 4, 425-436, 10.5194/amt-4-425-2011, 2011.

Coburn, S., Ortega, I., Thalman, R., Blomquist, B., Fairall, C. W., and Volkamer, R.: Measurements of diurnal variations and eddy covariance (EC) fluxes of glyoxal in the tropical marine boundary layer: description of the Fast LED-CE-DOAS instrument, Atmos. Meas. Tech., 7, 3579-3595, 10.5194/amt-7-3579-2014, 2014.

Coheur, P. F., Fally, S., Carleer, M., Clerbaux, C., Colin, R., Jenouvrier, A., Merienne, M. F., Hermans, C., and Vandaele, A. C.: New water vapor line parameters in the 26000-13000 cm^{-1} region, J. Quant. Spectrosc. Radiat. Transf., 74, 493-510, 10.1016/S0022-4073(01)00269-2, 2002.

Cuthbertson, C., and Cuthbertson, M.: The refraction and dispersion of neon and helium, P R Soc Lond a-Conta, 135, 40-47, DOI 10.1098/rspa.1932.0019, 1932.

Dixneuf, S., Ruth, A. A., Vaughan, S., Varma, R. M., and Orphal, J.: The time dependence of molecular iodine emission from Laminaria digitata, Atmos. Chem. Phys., 9, 823-829, 10.5194/acp-9-823-2009, 2009.

Everest, M. A., and Atkinson, D. B.: Discrete sums for the rapid determination of exponential decay constants, Rev. Sci. Instrum., 79, 023108-023109, 10.1063/1.2839918, 2008.

Fiedler, S. E., Hese, A., and Ruth, A. A.: Incoherent broad-band cavity-enhanced absorption spectroscopy, Chem. Phys. Lett., 371, 284-294, 10.1016/s0009-2614(03)00263-x, 2003.

Finley, B. D., and Saltzman, E. S.: Observations of Cl_2, Br_2, and I_2 in coastal marine air, J. Geophys. Res., 113, D21301, 10.1029/2008jd010269, 2008.

Fuchs, H., Dubé, W. P., Lerner, B. M., Wagner, N. L., Williams, E. J., and Brown, S. S.: A Sensitive and Versatile Detector for Atmospheric NO_2 and NO_x Based on Blue Diode Laser Cavity Ring-Down Spectroscopy, Environm. Sci. Technol., 43, 7831-7836, 10.1021/es902067h, 2009.

Gagliardi, G., and Loock, H.-P.: Cavity-Enhanced Spectroscopy and Sensing, 1 ed., Springer Series in Optical Sciences, 179, Springer, Berlin, Heidelberg, 10.1007/978-3-642-40003-2, 2014.

Gherman, T., Venables, D. S., Vaughan, S., Orphal, J., and Ruth, A. A.: Incoherent broadband cavity-enhanced absorption spectroscopy in the near-ultraviolet: Application to HONO and NO_2, Environm. Sci. Technol., 42, 890-895, 10.1021/es0716913, 2008.

Giver, L. P.: Intensity measurements of the CH_4 bands in the region 4350 Å to 10,600 Å, J. Quant. Spectrosc. Radiat. Transfer, 19, 311-322, 10.1016/0022-4073(78)90064-X, 1978.

545   He, Q., Bluvshtein, N., Segev, L., Meidan, D., Flores, J. M., Brown, S. S., Brune, W., and Rudich, Y.: Evolution of the Complex Refractive Index of Secondary Organic Aerosols during Atmospheric Aging, Environm. Sci. Technol., 52, 3456-3465, 10.1021/acs.est.7b05742, 2018.

Hoch, D. J., Buxmann, J., Sihler, H., Pöhler, D., Zetzsch, C., and Platt, U.: An instrument for measurements of BrO with LED-based Cavity-Enhanced Differential Optical Absorption Spectroscopy, Atmos. Meas. Tech., 7, 199-214, 10.5194/amt-7-199-2014, 2014.

550   Hohm, U.: Experimental determination of the dispersion in the main linear dipole polarizability α(ω) of small hydrocarbons and evaluation of Cauchy moments between 325 nm and 633 nm, Molecular Physics, 78, 929-941, 10.1080/00268979300100621, 1993.

Kahan, T. F., Washenfelder, R. A., Vaida, V., and Brown, S. S.: Cavity-Enhanced Measurements of Hydrogen Peroxide Absorption Cross Sections from 353 to 410 nm, J. Phys. Chem. A, 116, 5941-5947, 10.1021/jp2104616, 555   2012.

Karkoschka, E.: Spectrophotometry of the Jovian Planets and Titan at 300- to 1000-nm Wavelength: The Methane Spectrum, Icarus, 111, 174-192, 10.1006/icar.1994.1139, 1994.

King, L. V.: On the complex anisotropic molecule in relation to the dispersion and scattering of light, P R Soc Lond a-Conta, 104, 333-357, 10.1098/rspa.1923.0113, 1923.

560   Knight, G., Ravishankara, A. R., and Burkholder, J. B.: Laboratory studies of OBrO, J. Phys. Chem. A, 104, 11121-11125, 10.1021/jp002226u, 2000.

Langridge, J. M., Ball, S. M., and Jones, R. L.: A compact broadband cavity enhanced absorption spectrometer for detection of atmospheric NO$_2$ using light emitting diodes, Analyst, 131, 916-922, 10.1039/B605636A, 2006.

Langridge, J. M., Ball, S. M., Shillings, A. J. L., and Jones, R. L.: A broadband absorption spectrometer using light 565   emitting diodes for ultrasensitive, in situ trace gas detection, Rev. Sci. Instrum., 79, 123110, 10.1063/1.3046282, 2008.

McKendry, I. G., Christensen, E., Schiller, C., Vingarzan, R., Macdonald, A. M., and Li, Y.: Low Ozone Episodes at Amphitrite Point Marine Boundary Layer Observatory, British Columbia, Canada, Atmosphere-Ocean, 52, 271-280, 10.1080/07055900.2014.910164, 2014.

570   Min, K. E., Washenfelder, R. A., Dubé, W. P., Langford, A. O., Edwards, P. M., Zarzana, K. J., Stutz, J., Lu, K., Rohrer, F., Zhang, Y., and Brown, S. S.: A broadband cavity enhanced absorption spectrometer for aircraft measurements of glyoxal, methylglyoxal, nitrous acid, nitrogen dioxide, and water vapor, Atmos. Meas. Tech., 9, 423-440, 10.5194/amt-9-423-2016, 2016.

Naus, H., and Ubachs, W.: Experimental verification of Rayleigh scattering cross sections, Opt. Lett., 25, 347-349, 575   10.1364/ol.25.000347, 2000.

Nitschke, U., Dixneuf, S., Schmid, M., Ruth, A. A., and Stengel, D. B.: Contribution of living and degrading kelp to coastal iodine fluxes, Mar. Biol., 162, 1727-1738, 10.1007/s00227-015-2699-4, 2015.

Odame-Ankrah, C. A.: Improved detection instrument for nitrogen oxide species, Ph.D., Chemistry, University of Calgary, http://hdl.handle.net/11023/2006, 10.5072/PRISM/26475, Calgary, 2015.

580   Osthoff, H. D., Odame-Ankrah, C. A., Taha, Y. M., Tokarek, T. W., Schiller, C. L., Haga, D., Jones, K., and Vingarzan, R.: Low levels of nitryl chloride at ground level: Nocturnal nitrogen oxides in the Lower Fraser Valley of British Columbia, Atmos. Chem. Phys., 18, 6293-6315, 10.5194/acp-18-6293-2018, 2017.

585   Paul, D., and Osthoff, H. D.: Absolute Measurements of Total Peroxy Nitrate Mixing Ratios by Thermal
       Dissociation Blue Diode Laser Cavity Ring-Down Spectroscopy, Anal. Chem., 82, 6695-6703, 10.1021/ac101441z,
       2010.

       Peck, E. R., and Fisher, D. J.: Dispersion of argon, Journal of the Optical Society of America, 54, 1362-1364,
       10.1364/josa.54.001362, 1964.

       Peck, E. R., and Khanna, B. N.: Dispersion of nitrogen, Journal of the Optical Society of America, 56, 1059-1063,
       10.1364/josa.56.001059, 1966.

590   Penndorf, R.: Tables fo the refractive index for standard air and the Rayleigh scattering coefficient for the spectral
       region between 0.2 and 20.0 mu and their application to atmospheric optics, Journal of the Optical Society of
       America, 47, 176-182, 10.1364/josa.47.000176, 1957.

       Peters, C., Pechtl, S., Stutz, J., Hebestreit, K., Honninger, G., Heumann, K. G., Schwarz, A., Winterlik, J., and Platt,
       U.: Reactive and organic halogen species in three different European coastal environments, Atmos. Chem. Phys., 5,
595   3357-3375, 2005.

       Platt, U., and Stutz, J.: Differential Optical Absorption Spectroscopy: Principles and Applications, Physics of Earth
       and Space Environments Springer, New York, 2008.

       Saiz-Lopez, A., Plane, J. M. C., Baker, A. R., Carpenter, L. J., von Glasow, R., Gómez Martín, J. C., McFiggans, G.,
       and Saunders, R. W.: Atmospheric Chemistry of Iodine, Chem. Rev., 112, 1773-1804, 10.1021/cr200029u, 2012.

600   Savitzky, A., and Golay, M. J. E: Smoothing and Differentiation of Data by Simplified Least Squares Procedures,
       Anal. Chem., 36, 1627-1639, 10.1021/ac60214a047, 1964.

       Schuster, G., Labazan, I., and Crowley, J. N.: A cavity ring down/cavity enhanced absorption device for
       measurement of ambient NO_3 and N_2O_5, Atmos. Meas. Tech., 2, 1-13, 10.5194/amt-2-1-2009, 2009.

       Shardanand and Rao, A. D. P.: Absolute Rayleigh scattering cross sections of gases and freons of stratospheric
605   interest in the visible and ultraviolet regions, NASA TN D-8442, 1977.

       Sneep, M., and Ubachs, W.: Direct measurement of the Rayleigh scattering cross section in various gases, J. Quant.
       Spectrosc. Radiat. Transfer, 92, 293-310, 10.1016/j.jqsrt.2004.07.025, 2005.

       Sneep, M., Ityaksov, D., Aben, I., Linnartz, H., and Ubachs, W.: Temperature-dependent cross sections of O_2-O_2
610   collision-induced absorption resonances at 477 and 577 nm, J. Quant. Spectrosc. Radiat. Transf., 98, 405-424,
       10.1016/j.jqsrt.2005.06.004, 2006.

       Spietz, P., Gómez Martín, J. C., and Burrows, J. P.: Spectroscopic studies of the I_2/O_3 photochemistry: Part 2.
       Improved spectra of iodine oxides and analysis of the IO absorption spectrum, J. Photochem. Photobiol. A, 176, 50-
       67, 10.1016/j.jphotochem.2005.08.023, 2005.

615   Spietz, P., Gómez Martín, J., and Burrows, J. P.: Effects of column density on I_2 spectroscopy and a determination
       ofI$_2$ absorption cross section at 500 nm, Atmos. Chem. Phys., 6, 2177-2191, 10.5194/acp-6-2177-2006, 2006.

       Thalman, R., and Volkamer, R.: Temperature dependent absorption cross-sections of O_2-O_2 collision pairs between
       340 and 630 nm and at atmospherically relevant pressure, Phys. Chem. Chem. Phys., 15, 15371-15381,
       10.1039/c3cp50968k, 2013.

620   Thalman, R., Zarzana, K. J., Tolbert, M. A., and Volkamer, R.: Rayleigh scattering cross-section measurements of
       nitrogen, argon, oxygen and air, J. Quant. Spectrosc. Radiat. Transfer, 147, 171-177, 10.1016/j.jqsrt.2014.05.030,
       2014.

625   Thalman, R., Baeza-Romero, M. T., Ball, S. M., Borrás, E., Daniels, M. J. S., Goodall, I. C. A., Henry, S. B., Karl, T., Keutsch, F. N., Kim, S., Mak, J., Monks, P. S., Muñoz, A., Orlando, J., Peppe, S., Rickard, A. R., Ródenas, M., Sánchez, P., Seco, R., Su, L., Tyndall, G., Vázquez, M., Vera, T., Waxman, E., and Volkamer, R.: Instrument intercomparison of glyoxal, methyl glyoxal and NO_2 under simulated atmospheric conditions, Atmos. Meas. Tech., 8, 1835-1862, 10.5194/amt-8-1835-2015, 2015.

Thalman, R. M., and Volkamer, R. M.: Inherent calibration of a blue LED-CE-DOAS instrument to measure iodine oxide, glyoxal, methyl glyoxal, nitrogen dioxide, water vapour and aerosol extinction in open cavity mode, Atmos.
630   Meas. Tech., 3, 1797-1814, 10.5194/amt-3-1797-2010, 2010.

Tokarek, T. W., Brownsey, D. K., Jordan, N., Garner, N. M., Ye, C. Z., Assad, F. V., Peace, A., Schiller, C. L., Mason, R. H., Vingarzan, R., and Osthoff, H. D.: Biogenic emissions and nocturnal ozone depletion events at the Amphitrite Point Observatory on Vancouver Island, Atmosphere-Ocean, 55, 121-132, 10.1080/07055900.2017.1306687, 2017.

635   Triki, M., Cermak, P., Méjean, G., and Romanini, D.: Cavity-enhanced absorption spectroscopy with a red LED source for NOx trace analysis, Applied Physics B: Lasers and Optics, 91, 195-201, 10.1007/s00340-008-2958-x, 2008.

Vaughan, S., Gherman, T., Ruth, A. A., and Orphal, J.: Incoherent broad-band cavity-enhanced absorption spectroscopy of the marine boundary layer species I_2, IO and OIO, Phys. Chem. Chem. Phys., 10, 4471-4477,
640   10.1039/b802618a, 2008.

Voigt, S., Orphal, J., and Burrows, J. P.: The temperature and pressure dependence of the absorption cross-sections of NO_2 in the 250-800 nm region measured by Fourier-transform spectroscopy, Journal Of Photochemistry And Photobiology A-Chemistry, 149, 1-7, 10.1016/S1010-6030(01)00650-5, 2002.

Washenfelder, R. A., Langford, A. O., Fuchs, H., and Brown, S. S.: Measurement of glyoxal using an incoherent
645   broadband cavity enhanced absorption spectrometer, Atmos. Chem. Phys., 8, 7779-7793, 10.5194/acp-8-7779-2008, 2008.

Washenfelder, R. A., Flores, J. M., Brock, C. A., Brown, S. S., and Rudich, Y.: Broadband measurements of aerosol extinction in the ultraviolet spectral region, Atmos. Meas. Tech., 6, 861-877, 10.5194/amt-6-861-2013, 2013.

Washenfelder, R. A., Attwood, A. R., Flores, J. M., Zarzana, K. J., Rudich, Y., and Brown, S. S.: Broadband cavity-
650   enhanced absorption spectroscopy in the ultraviolet spectral region for measurements of nitrogen dioxide and formaldehyde, Atmos. Meas. Tech., 9, 41-52, 10.5194/amt-9-41-2016, 2016.

Watson, J., and Estes, J. A.: Stability, resilience, and phase shifts in rocky subtidal communities along the west coast of Vancouver Island, Canada, Ecol. Monogr., 81, 215-239, 10.1890/10-0262.1, 2011.

Werle, P., Mucke, R., and Slemr, F.: The Limits of Signal Averaging in Atmospheric Trace-Gas Monitoring by
655   Tunable Diode-Laser Absorption-Spectroscopy (TDLAS), Applied Physics B-Photophysics and Laser Chemistry, 57, 131-139, 10.1007/BF00425997, 1993.

Wu, T., Zha, Q., Chen, W., Xu, Z., Wang, T., and He, X.: Development and deployment of a cavity enhanced UV-LED spectrometer for measurements of atmospheric HONO and NO_2 in Hong Kong, Atmos. Environm., 95, 544-551, 10.1016/j.atmosenv.2014.07.016, 2014.
660
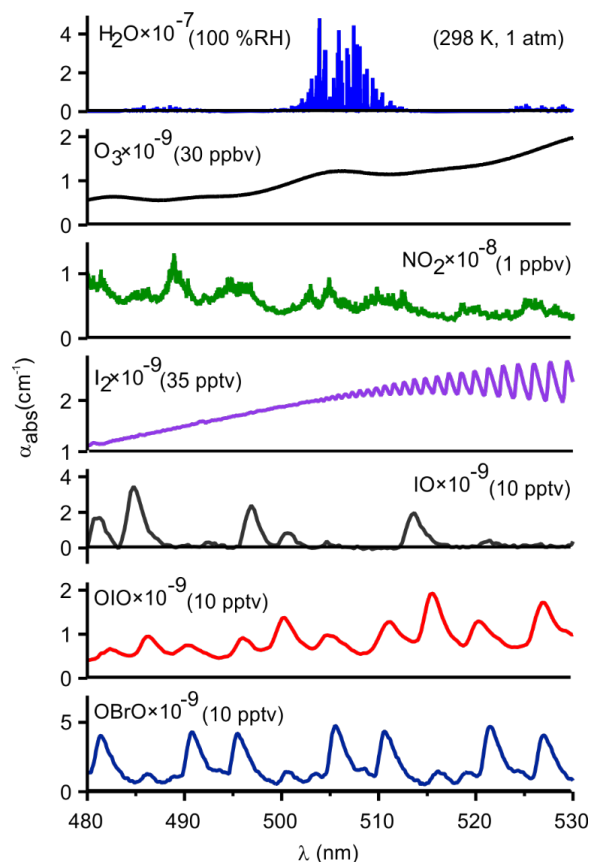
Figure 1. Absorption coefficients for atmospheric absorbers in the cyan region at typical tropospheric abundances (stated in brackets after each species). Absorption cross-sections were downloaded from the Max-Planck Institute for Chemistry's web site located at www.uv-vis-spectral-atlas-mainz.org and are based on the following: H_2O (Coheur et al., 2002), O_3 (Burkholder and Talukdar, 1994), NO_2 (Voigt et al., 2002), I_2 (Spietz et al., 2006), IO, OIO (Spietz et al., 2005), and OBrO (Knight et al., 2000). The absorption cross-section of O_4 is shown in Figure S4.
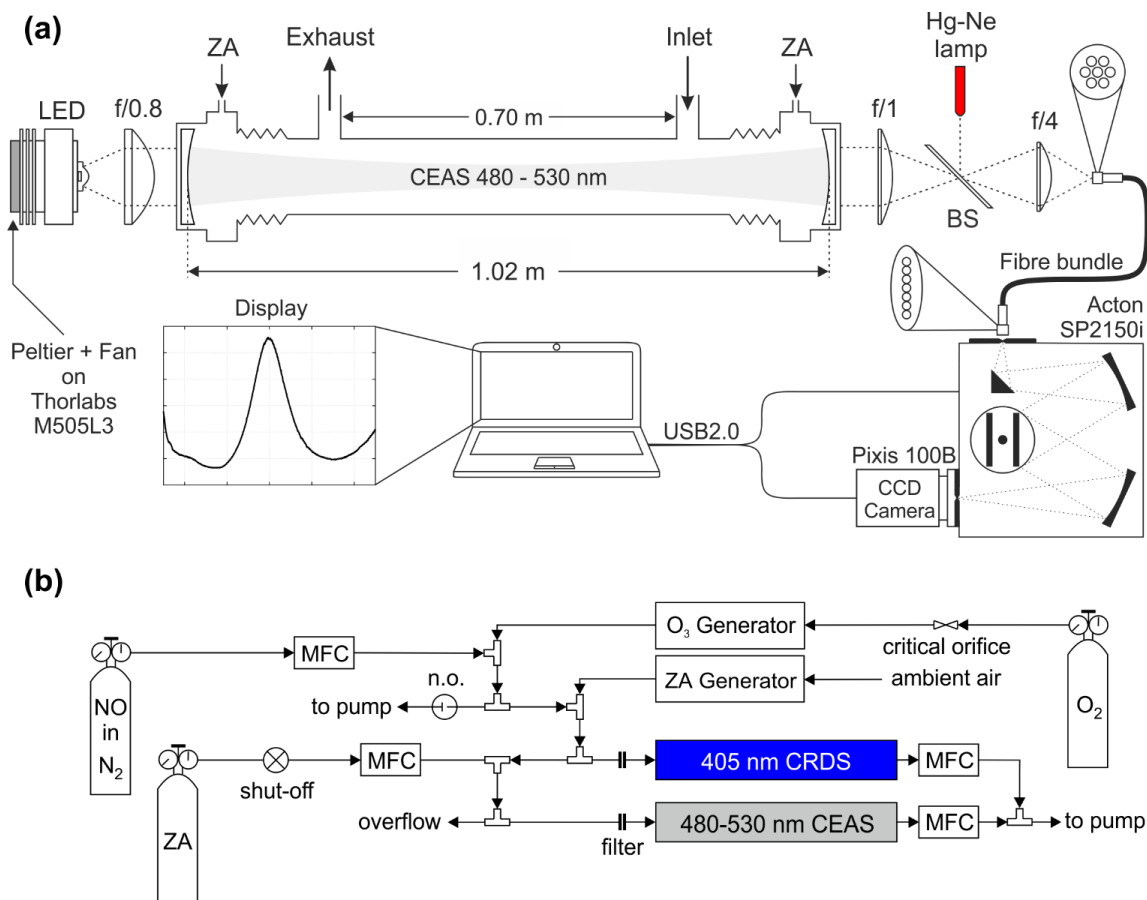
Figure 2. (a) Setup of the cyan CEAS (not to scale). (b) Setup of NO$_2$ calibration gas delivery for instrument characterization experiments. Abbreviations: LED – light emitting diode, BS – quartz beam splitter, CCD – charge-coupled device, ZA – zero air, USB – universal serial bus, and MFC – mass flow controller.
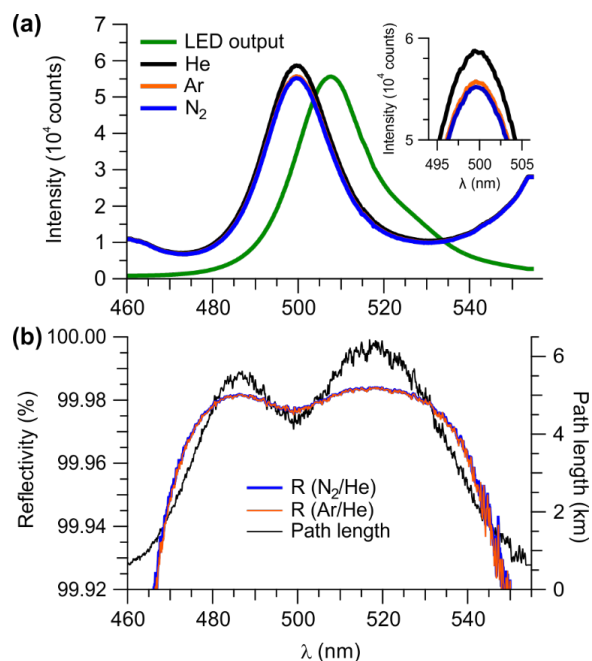
Figure 3. (**a**): Transmission spectra (averaged over 15 min) observed when the sample cell was filled with He, Ar, or
N$_2$. The LED output spectrum (in arbitrarily scaled units) is superimposed. (**b**): Mirror reflectivity and effective path
length (based on Ar/He) calculated from the data shown in panel (a).
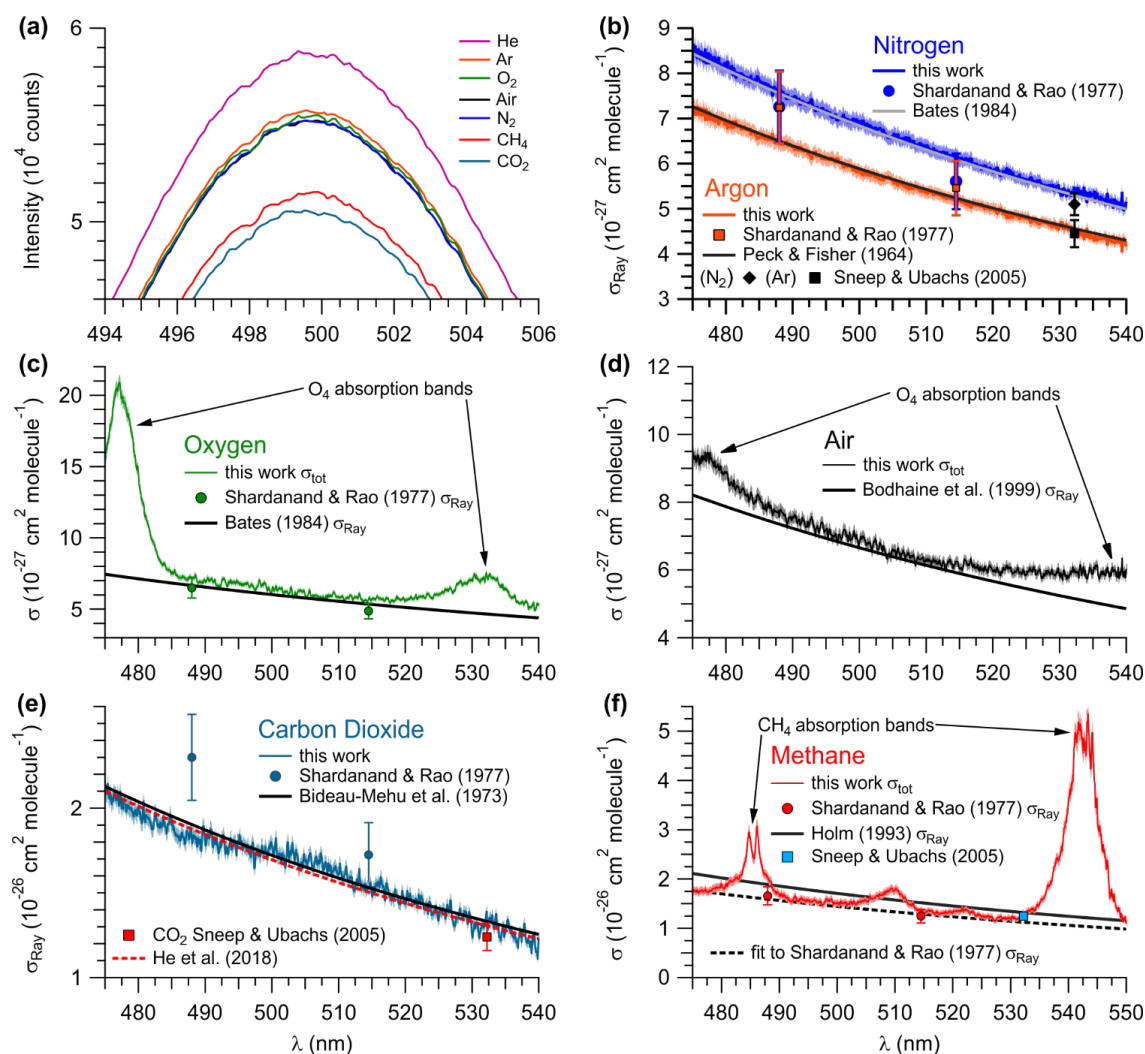
Figure 4. Measurements of pure gases. **(a)** Relative intensities of the CEAS signal due to each sampled gas. Extinction cross-sections of **(b)** 99.998% N_2 (shown in blue) and 99.998% Ar (red), **(c)** air (black), **(d)** 99.99% O_2 (green), **(e)** 99.95% CO_2 (teal), and **(f)** 99.97% CH_4 (red). Shaded areas represent ±2.5% error margin in N_2, Ar, O_2, air, and CO_2, and 4.6% in CH_4. σ_{Ray} - Rayleigh scattering cross-section; σ_{tot} = total extinction cross-section ($=\sigma_{Ray} + \sigma_{abs}$).
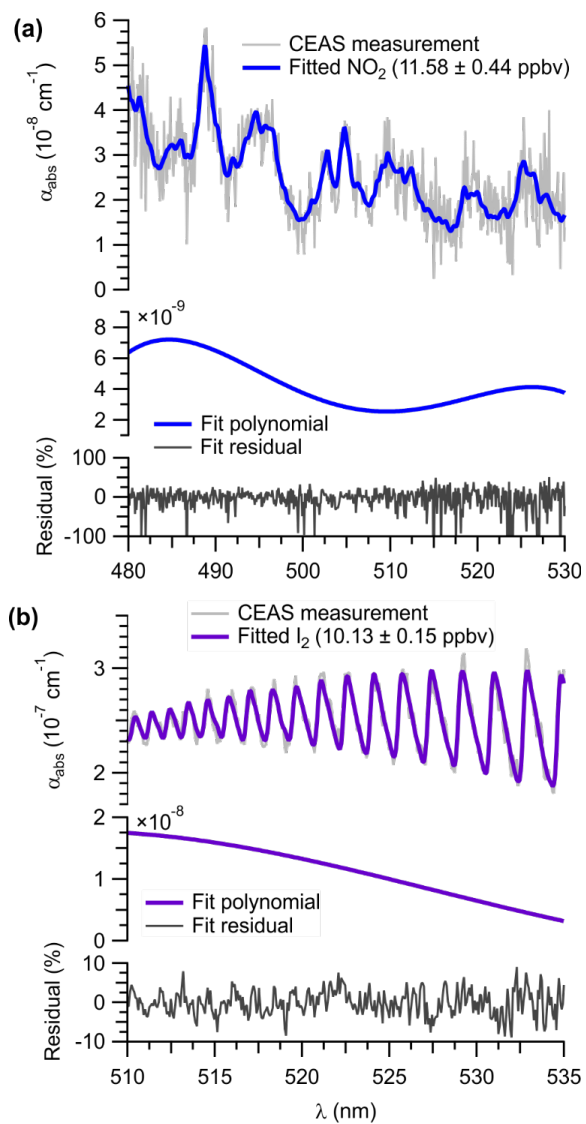
Figure 5. Spectral fits to 60 s CEAS signal, including a 3rd order polynomial and fit residual, for **a)** NO$_2$ (ambient)
and **b)** I$_2$ (calibration) during the ORCA field campaign.
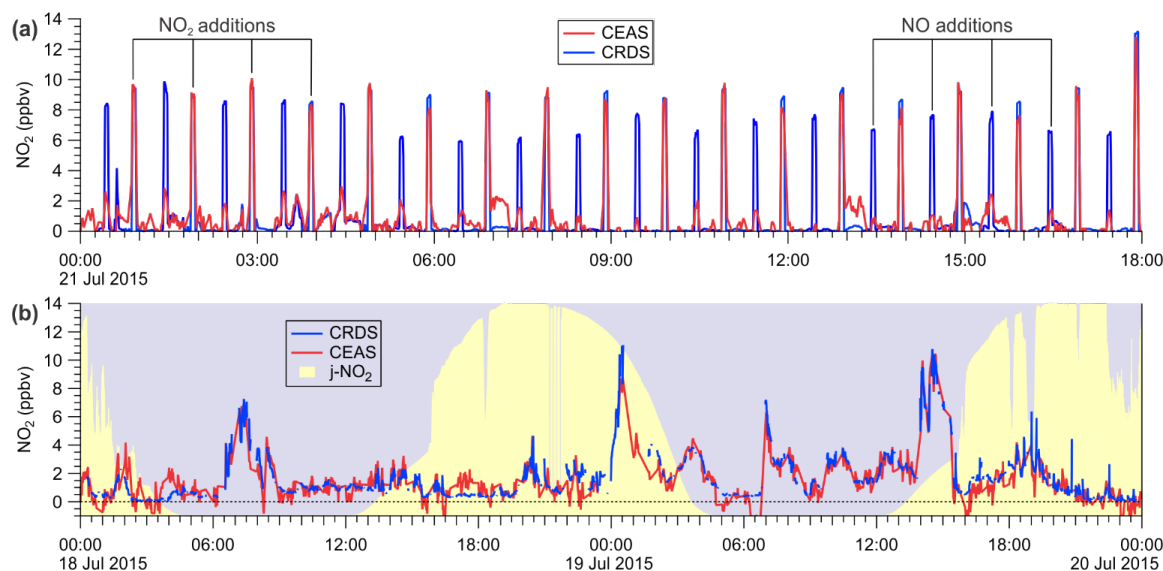
Figure 6. (a) Sample time series of continuous CEAS and CRDS data collected during the ORCA campaign showing measurements of ambient air, NO_2-free "zero" air (every 30 min), and hourly standard additions of NO_2 (~10 ppbv) in "zero air" and NO (~130 ppbv) to ambient air. When high concentrations of NO were added, more NO_2 was observed by CRDS due to this instrument's longer inlet residence time. **(b)** Sample time series of ambient air NO_2 mixing ratios observed by CEAS and CRDS during ORCA.
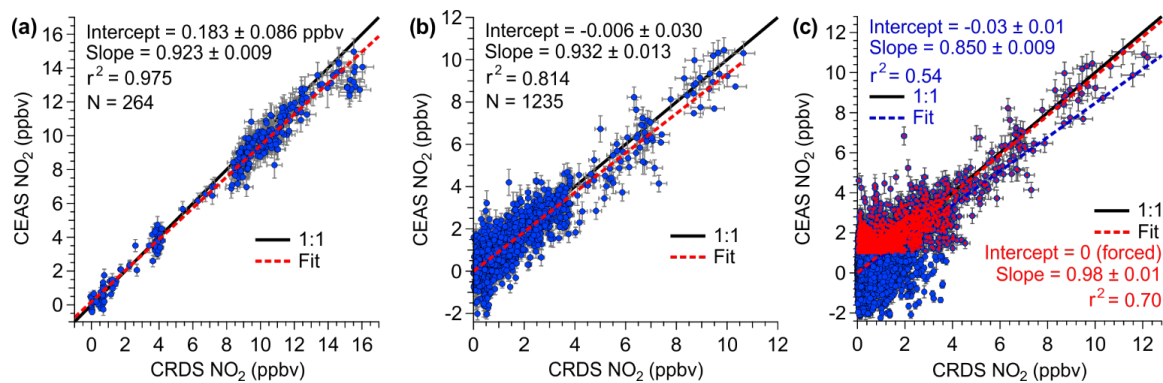
Figure 7. Scatter plots and straight-line fits of CEAS and CRDS NO_2 mixing ratios for: **(a)** standard additions and calibrations, **(b)** ambient air measurements on 18-19 Jul, 2015, and **(c)** ambient air measurements of the entire campaign. For the fit line shown in red, CEAS retrievals with NO_2 mixing ratios <1 ppbv were excluded. All data were averaged to 60 s.

695

700
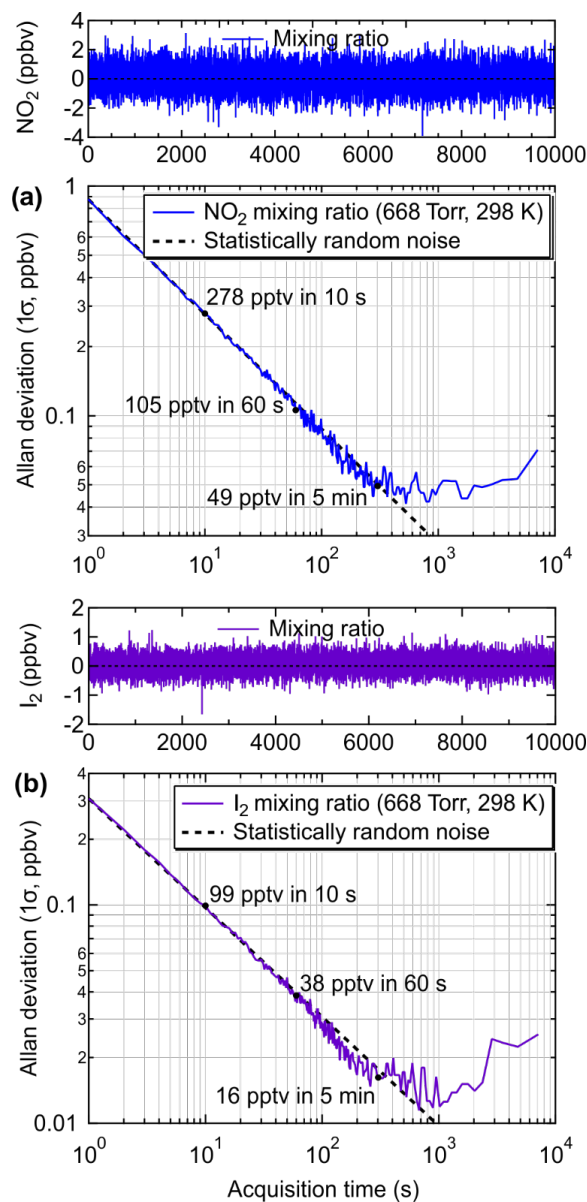
Figure 8. Allan deviation plots of data collected while the CEAS was sampling zero air to determine the optimum integration time of: (**a**) the calculated NO_2 mixing ratios at 668 Torr (1.5 slpm sample rate) and 298 K, and (**b**) the calculated I_2 mixing ratios under the same conditions.

705

Table 1. Summary of observed and *n*-based Rayleigh scattering cross-sections.

Gas (Purity)	λ (nm)	σ_{Ray} (this work)[a] (10^{-27} cm² molecule^{-1})	σ_{Ray} (*n*-based)[b] (10^{-27} cm² molecule^{-1})	σ_{Ray} (CRDS)[d] (10^{-27} cm² molecule^{-1})	$(n-1) \times 10^{-6}$	F_k[c]
N$_2$ (99.998%)	485.03	7.85	7.74	-	284.97	
	495.08	7.16	7.12	-	284.70	
	505.01	6.61	6.56	-	284.45	1.034
	515.06	6.09	6.06	-	284.22	
	525.07	5.61	5.60	-	283.99	
	532.20	5.49	5.30	5.1(±0.2)	283.84	
O$_2$ (99.99%)	485.03	-	6.83	-	273.34	
	495.08	6.84	6.28	-	273.03	
	505.01	5.96	5.78	-	272.74	1.096
	515.06	5.72	5.33	-	272.46	
	525.07	-	4.93	-	272.21	
Air[e]	485.03	-	7.54	-	279.38	
	495.08	7.22	6.93	-	279.10	
	505.01	6.60	6.39	-	278.84	1.133
	515.06	6.04	5.89	-	278.59	
	525.07	-	5.45	-	278.36	
Ar (99.998%)	485.03	6.58	6.67	-	269.02	
	495.08	6.10	6.13	-	268.77	
	505.01	5.61	5.65	-	268.54	1.000
	515.06	5.19	5.22	-	268.31	
	525.07	4.81	4.82	-	268.11	
	532.20	4.40	4.56	4.4 (±0.3)	267.97	
CO$_2$ (99.97%)	485.03	19.0	19.5	-	429.81	
	495.08	18.0	17.9	-	429.33	
	505.01	16.9	16.5	-	428.88	1.136
	515.06	14.7	15.2	-	428.46	
	525.07	13.7	14.1	-	428.06	
	532.20	13.9	13.3	12.4(±0.8)	427.79	
CH$_4$ (99.95%)	492.06	15.4	15.4[f]	-	483.22	
	497.46	14.7	14.7[f]	-	482.87	
	501.72	14.5	14.2[f]	-	482.59	1.000
	516.92	12.8	12.6[f]	-	481.66	
	527.28	11.6	11.7[f]	-	481.08	
	532.20	13.1	13.2[f]	12.5(±0.2)	480.81	

[a] The absolute uncertainty is ±2.5% (see Sect. 4.1); [b,c] See text for references of *n*-based scattering cross-sections and references therein for corresponding calculations of King correction factors; [d] From (Sneep and Ubachs, 2005);

uncertainty is stated as 1σ. [e] The ratio of N_2/O_2 in the cylinder was $\sim$ 80.5/19.5; [f] Comparison is to the fitted expression

710   to the data set of (Shardanand and Rao, 1977).

Table 2. Selected CEAS detectors for quantification of NO$_2$ in the near-UV and visible region of the electromagnetic spectrum

	Arc 330 (Washenfelder et al., 2016)	Violet 365 (Gherman et al., 2008)	Blue 455 (Min et al., 2016)	Blue 455 (Langridge et al., 2006)	Blue 465 (Thalman and Volkamer, 2010)	Red 643 (Triki et al., 2008)	Red 660 (Wu et al., 2014)	Cyan 508 (This work)
Light source manu-facturer	Energetiq	Omicron Latronics	LEDEngin	Lumileds Luxeon	LEDEngin	Lumileds Luxeon	Marubeni America	Thorlabs
model	Laser-driven arc lamp	n/a	LZ1-00DB05	LXHL–PR09	LZ1–00DB05	LXHL–MD1D	SMB660N-1100	M505L3
optical power (W)	125 W	0.105	1	0.450	1.0	0.190	0.300	0.440
$\lambda_p \pm$FWHM[a] (nm)	n/a	365±12	460±5	455±20	465±22	643±20	660±14	508±30
Fit range(s) (nm)	315-350	366 – 378	438 – 468	441 – 463	435 – 465 455 – 487	640 – 670	353 – 376	480 – 530
Mirror reflectivity (%)	99.93	99.94	99.997	99.976	99.9964	99.991	99.925	99.9998
Cell length (m)	1.00	1.15 and 4.50	0.48	1.50	0.99	2.00	1.76	1.02
Path length[b] (km)	1.43	1.9 and 7.5	17.8	6.25	27.5	22	2.1	510
Integration time (s)	30	600	5	30	60	60	120	60
LOD (1σ, ppbv)	0.14#	0.38*	0.04#	0.10*	0.030	9.0*	1	0.11* 0.53#

[a] peak wavelength + full-width at half maximum; [b] effective path length, L$_{eff}$ = 1/(1-R); * laboratory sample; # field samples

715